A solar tornado triggered by flares?

N. K. Panesar[1,2], D. E. Innes[1], S. K. Tiwari[1], and B. C. Low[3]

[1] Max-Planck Institut für Sonnensystemforschung, Max-Planck-Str. 2, 37191 Katlenburg-Lindau
[2] Institut für Astrophysik, Georg-August-Universität Göttingen, Friedrich-Hund-Platz 1, D-37077 Göttingen
[3] High Altitude Observatory, National Center for Atmospheric Research, P.O. Box 3000, Boulder, CO 80307, USA

Preprint online version: November 29, 2012

ABSTRACT

Context. Solar tornados are dynamical, conspicuously helical magnetic structures mainly observed as a prominence activity.
Aims. We investigate and propose a triggering mechanism for the solar tornado observed in a prominence cavity by SDO/AIA on September 25, 2011.
Methods. High-cadence EUV images from the SDO/AIA and the Ahead spacecraft of STEREO/EUVI are used to correlate three flares in the neighbouring active-region (NOAA 11303), and their EUV waves, with the dynamical developments of the tornado. The timings of the flares and EUV waves observed on-disk in 195Å are analyzed in relation to the tornado activities observed at the limb in 171Å.
Results. Each of the three flares and its related EUV wave occurred within 10 hours of the onset of the tornado. They have an observed causal relationship with the commencement of activity in the prominence where the tornado develops. Tornado-like rotations along the side of the prominence start after the second flare. The prominence cavity expands with acceleration of tornado motion after the third flare.
Conclusions. Flares in the neighbouring active region may have affected the cavity prominence system and triggered the solar tornado. A plausible mechanism is that the active-region coronal field contracted by the 'Hudson effect' due to the loss of magnetic energy as flares. Subsequently the cavity expanded by its magnetic pressure to fill the surrounding low corona. We suggest that the tornado is the dynamical response of the helical prominence field to the cavity expansion.

Key words. Sun: chromosphere – Sun: prominences – Sun: flares – Sun: coronal cavity

1. Introduction

Prominences consist of relatively large, cool and over dense plasma seen in the lower corona above the solar limb (Martin 1998; Tandberg-Hanssen 1995; Mackay et al. 2010). Their structure and composition are exceedingly complicated. The plasma mainly resides in highly tangled magnetic fields (van Ballegooijen & Cranmer 2010). Coronal cavities are often observed to have cooler prominence plasma at their bases (Hudson et al. 1999; Gibson et al. 2006; Régnier et al. 2011). The cavity is a region of relatively low density, high temperature plasma (Gibson et al. 2010; Habbal et al. 2010). Berger et al. (2011) have proposed that the prominence and its cavity are a form of magneto-thermal convective structure, macroscopically stable but internally in a constant state of ubiquitous motions (Low et al. 2012a,b).

Viewed at the limb, quiescent prominences mostly appear as curtains of vertical thread-like structures (Berger et al. 2008). Occasionally they look like tornados with rotations along, or of, their magnetic structures (Pettit 1943; Liggett & Zirin 1984). At first glance it is not obvious why tornados do not erupt but continue rotating for several hours before quietening down. Recently, images from Atmospheric Imaging Assembly (AIA) on the Solar Dynamic Observatory (SDO), have allowed the study

of solar tornados (Li et al. 2012; Su et al. 2012; Liu et al. 2012a). The driving mechanism may be a coupling and expansion of a twisted flux rope into the coronal cavity (Li et al. 2012) and/or related to photospheric vortices at the footpoint of the tornado (Attie et al. 2009; Wedemeyer-Böhm et al. 2012; Su et al. 2012).

This letter is a study of the impressive solar tornado observed by AIA on 25 September 2011. Li et al. (2012) described the formation and disappearance of the related prominence by analysing SDO data from 24-26 September. The evolution of the tornado was attributed to the expansion of helical structures into the cavity. But the reason behind the expansion remained an open question.

Here we analyze observations on the mechanism leading to the expansion of the prominence. We show using Solar TErrestrial RElations Observatory (STEREO) Extreme UltraViolet Imager (EUVI) observations that three strong flares in a neighbouring active region coincided with phases of the tornado activation. Each flare was associated with a Coronal Mass Ejection (CME) and EUV wave. Particularly, after the third flare, there was slow but significant expansion of the overlying prominence cavity together with more rapid rotation at the top of the prominence. We describe the observations in Section 2. The evolution of the tornado, its relationship to the solar flares and EUV waves are described in Section 3. In Section 4, we summarize our observations and speculate on the link between the flares and the cavity expansion.
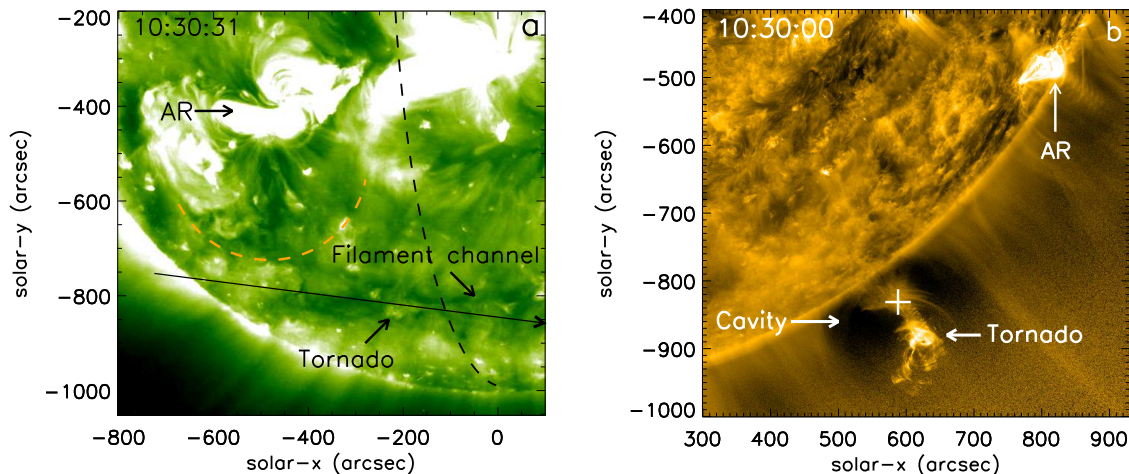
Fig. 1. The region around a tornado on 25 September 2011: a) EUVI-A 195Å; b) AIA 171Å images. On the EUVI image, the black dashed line shows the position of the AIA limb, and the long diagonal arrow is the epipolar line for the prominence position marked with '+' on the AIA image. The orange dashed line outlines the position of the southern edge of the AR corona.

2. Observations

The solar tornado on 25 September 2011 was observed on the south west limb by SDO/AIA (Lemen et al. 2012). In images from EUVI on the Ahead spacecraft of STEREO (Howard et al. 2008), it appeared on the solar disk around 15° E. The separation angle between SDO and STEREO-A was 103°. We study the tornado by combining observations from the two directions.

AIA takes high spatial resolution ($0.6''$ pixel^{-1}) full disk images with a cadence of 12 s. For the analysis, we select images from the 171Å channel which is centered on the Fe IX line formed around 0.63 MK. Images from this channel show both hot, bright emitting and cold, dense absorbing parts of the prominence, as well as the dark, low density cavity and the surrounding coronal loops. To enhance the visibility of the cavity and faint loops, we removed an average background from the 171Å images by taking the median of two months data - September and October, 2011.

During the period studied, 01:30-13:30 UT, SDO was in eclipse from 06:02-07:13 UT. This gap is covered by the SWAP instrument on PROBA-2 (Halain et al. 2010). SWAP provides a full Sun 174Å image every 2-3 min with a spatial resolution of $3.16''$ pixel^{-1}. The images are not as detailed as AIA images but are essential for checking the behaviour of the prominence during the data gap.

The EUVI-A 195Å images have a time cadence of 5 min and resolution of $1.6''$ pixel^{-1}. The 195Å emission is mainly Fe XII formed at ∼1.2 MK. To confirm the prominence position in the EUVI images, we obtained the three-dimensional coordinates of the prominence with the routine SCC_MEASURE (Thompson 2009) available in the SolarSoft library.

2.1. Overview

In Fig. 1 we show the EUVI-A 195Å and AIA 171Å images of the filament/prominence and the active region NOAA 11303 (marked with an arrow) as seen from the two angles. The position of the cross on the stem of the prominence lies along the epipolar line drawn as a long black arrow on the EUVI image. The dark lane crossed by the epipolar line is the filament channel and the tornado is the bright region that coincides with the epipolar line and the filament channel, indicated with a black arrow. The core of

the active region is separated by $300''$ from the filament channel. However, the southern edge of the active region corona (outlined by orange dashed line) reaches to within $50''$ of the filament channel.

2.2. The three flares

There were flares at approximately 02:45, 07:00, 09:40 UT from the nearby active region. They were all associated with CMEs and EUV waves. The third was GOES class M1.4 according to the NOAA flare catalogue[1]. The GOES class of the first two are not given in the catalogue. We therefore checked the hard X-ray quicklook images from the Reuven Ramaty High Energy Solar Spectroscopic Imager (RHESSI). Unfortunately they both had their peaks during RHESSI data gaps. The first RHESSI image in the flares' decay phase showed that these flares were the brightest RHESSI sources. At the time of the first and second flares the GOES 1-8Å fluxes reached the M4.4 and M1.0 level respectively, so it is possible that these too were M-class flares.

The flares' onsets and related EUV waves can be seen in the 195Å running ratio images shown in Fig. 2. The running ratio images are the log of the intensity at the time shown on the images divided by the intensity 5 min earlier. Because this reflects relative changes the faint EUV waves show up against bright inactive active regions. The faint EUV wavefronts sweep over the filament channel about half an hour after the flare (bottom row). The small white arrows point to the tornado site where there was increased activity along the filament channel after the flares.

When we take a time series along the orange dashed line drawn on Fig. 2e, we are able to see the relation between the EUV waves and the filament activity (Fig. 3). In this time series image, the waves associated with the three flares are marked by F1, F2 and F3 and a red arrow points to the filament activity. We note that the filament activity associated with F2 increased before the arrival of the EUV wave. We also notice that each EUV wave front was followed by a series of oscillations with a period of 20 min at the edge of the active region and along the filament channel. Similar post-EUV cavity oscillations, seen at the limb

---

[1] ftp://ftp.ngdc.noaa.gov/STP/space-weather/solar-data/solar-features/solar-flares/x-rays/goes
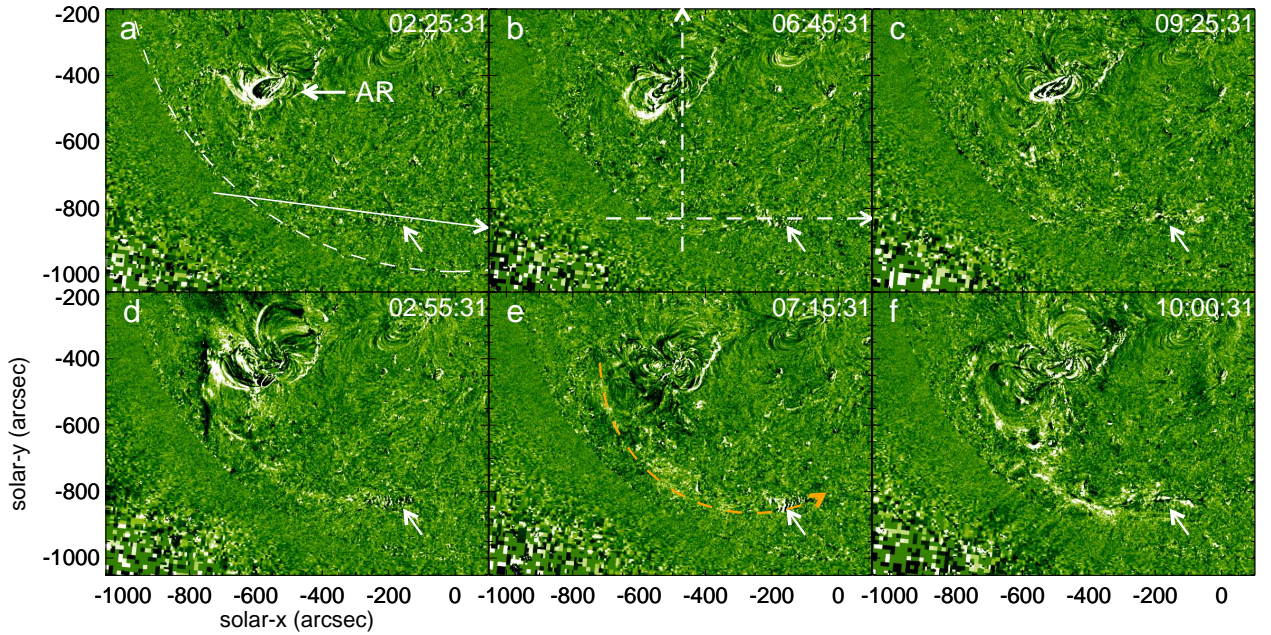
Fig. 2. EUVI-A 195Å running ratio images showing the onset of the three flares (a,b,c) and their associated EUV waves (d,e,f). In (a) the epipolar line shown in Fig. 1a is drawn as a long white arrow, and the solar limb is drawn as a dashed white line. The small white arrow in all images points to the tornado site. The dot-dashed/dashed lines in (b) mark the positions of time series shown in Fig. 4, and the orange dashed line along the EUV wave front in (e) the position of the time series in Fig. 3.
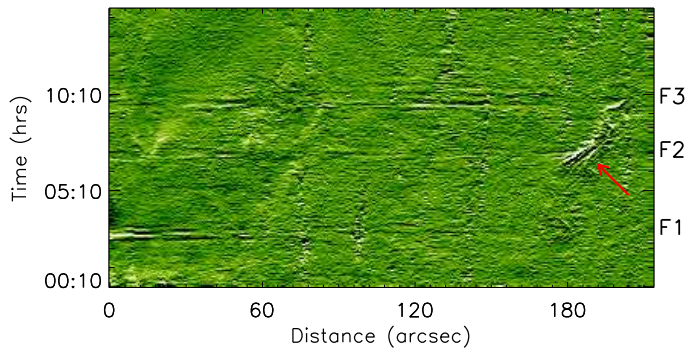

Fig. 3. EUVI 195Å running ratio space time image along the dashed line in Fig. 2e. Three flares are labelled as F1, F2 and F3. The red arrow points to the filament.

in AIA images, have been reported by Liu et al. (2012b). EUVI images have a much lower cadence than AIA, and may not be resolving the wave trains.

As mentioned above, the EUV wave reached the filament channel after the filament activation. To investigate whether the activation could have been triggered by the flare, we took time series through the flare sites (vertical line Fig. 2b) and along the filament channel across the activated filament (horizontal line in Fig. 2b). We observe that there are perturbations in the filament plasma immediately after each flare (yellow arrows in Fig. 4b). Large-scale changes along the filament channel started after F2 and increased further after the F3.

The reaction of the prominence to the flares is illustrated in Fig. 7. The positions of the three time series are drawn on Fig. 6, an AIA image of the active region and tornado. The oscillations of the prominence at the time of F1 (Fig. 7a) are consistent with a flare trigger from the

north since it moved first towards the pole. The wobbling in the prominence after the flare is also clearly visible in the movie6a (Fig. 6).

The second flare, F2, was at ∼06:45 UT when SDO was in eclipse. Since this phase is important for understanding the tornado, we checked the SWAP data to see if the prominence activation started before F2. The SWAP data are shown in the movie attached with Fig. 5. Although the SWAP images are not as sharp as AIA images, they show quite clearly that increased prominence activity occurred after F2 and that the first AIA images after eclipse caught the expansion of the flare loops and the rapid growth in prominence activity. The middle image in Fig. 7b, taken along the dashed line in Fig. 6, shows an arm of prominence plasma reaching out in the direction of the active region. There is also a very slight expansion of the cavity boundary towards the active region.

The biggest change in the cavity occurred after F3 when the bright and complex top part of the prominence started to rotate faster. The movie6b attached to Fig. 6, shows the evolution of the tornado and flare from F2 to a couple of hours after F3. The time series in Fig. 7c, taken along the top white arrow in Fig. 6, shows the main features. The flare erupted at 09:20 UT. The active region loops started expanding at 09:40:48 UT. At 09:50:13 UT there was a sharp contraction, approximately 10 Mm, of the observed cavity. The cavity started expanding back towards the active region after ∼10:00 UT. It grows from 140 Mm to 167 Mm in 3.5 hours. At the same time, the prominence grew in height and the bright and complex head of the prominence started to rotate faster, forming the tornado. The rotations at the top of the prominence/tornado lasted ∼3.5 hours with a speed from 55 km s^{-1} to 95 km s^{-1} (Li et al. 2012).
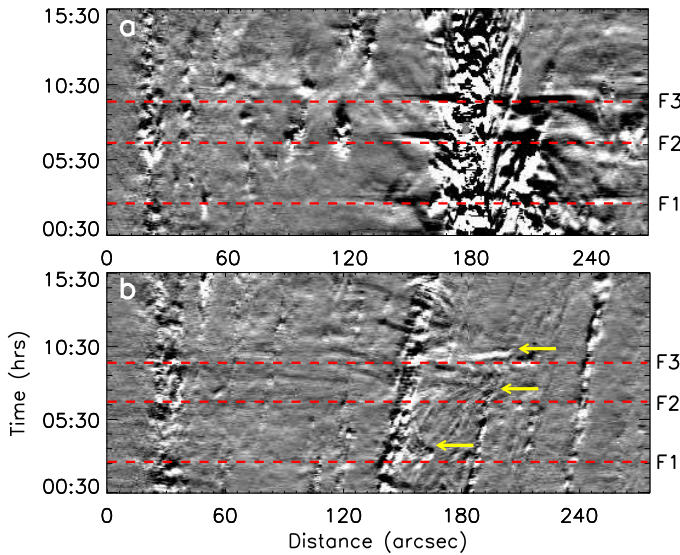
Fig. 4. EUVI 195Å running difference time series along (a) the vertical and (b) the horizontal line in Fig. 2b. The red dashed lines are drawn at the flare F1, F2, and F3 times. In b) the yellow arrows point to the changes in filament structure after the flares.
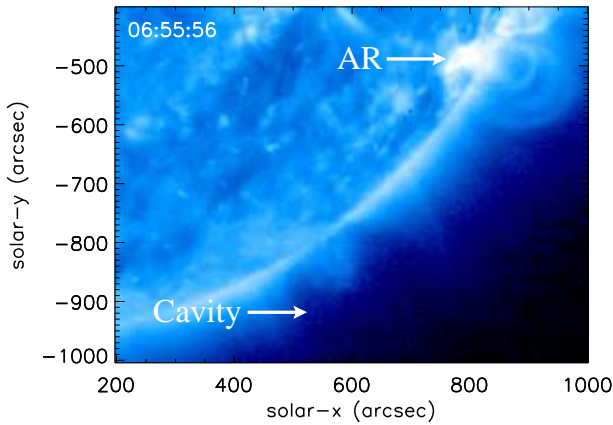

Fig. 5. SWAP 174Å intensity image from 25 September 2011. The arrows show the positions of the cavity and the active region (AR). This frame is taken from the movie-"MOVIE5.mp4".

3. Discussion

A solar tornado was observed by AIA and EUVI-A on 25 September 2011. The tornado was reported by Li et al. (2012), who attributed it to the growth of a helical prominence system. The reason for the prominence growth remained unanswered. After careful observation of the event using AIA full disk images, we noticed that AR 11303, to the north of the prominence cavity was flaring and suspected it of having influenced the prominence in some way. We observed three flares, and they were all associated with EUV waves that swept over the prominence cavity. Each time the cavity was buffeted by the wave, the prominence plasma became more active. After the third flare a tornado had developed at the top of the prominence.

After the first flare, there were clear oscillations along the prominence stem. The second flare caused plasma to move along arm-like extensions projecting out from the
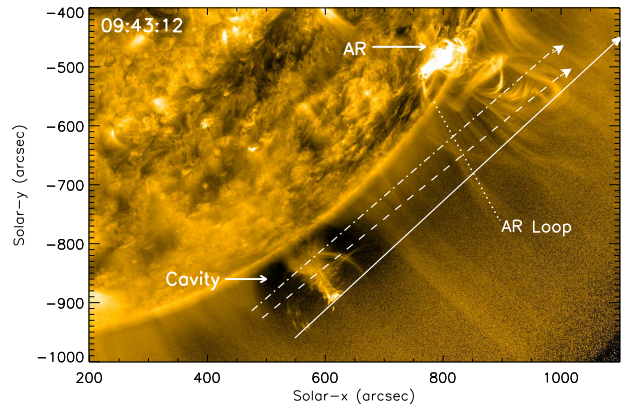

Fig. 6. AIA 171Å intensity image. The diagonal long arrows show the positions of the time series images through the prominence/tornado, cavity, active region hot loop (AR loop) and active region (AR) shown in Fig. 7. This is the frame from the movie-"MOVIE6b.mp4". "MOVIE6a.mp4" shows the evolution of this region at earlier times.
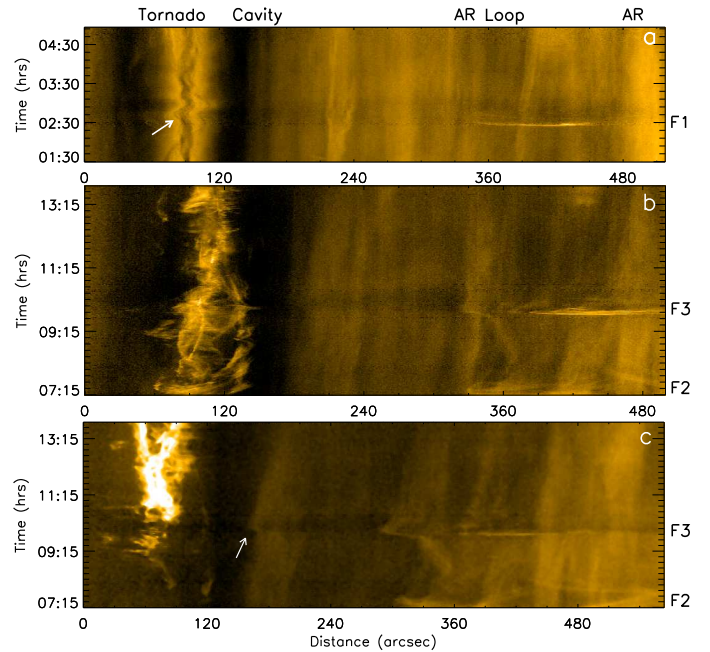

Fig. 7. AIA 171Å intensity time series along the diagonal arrows in Fig. 6: a) oscillations of the prominence stem triggered by F1 taken along bottom white arrow; b) activity triggered by F2 and F3 taken along the middle white arrow; c) tornado activity and cavity changes triggered by F2 and F3 taken along top arrow. The arrow at the time of the flare (~09.40 UT) points to the movement of the cavity boundary.

stem in the direction of the active region. These extensions appear to subsequently rotate back towards the prominence before the third flare. After the third flare the tornado became very strong and was stable for about 3.5 hours. The third flare seemed to have the biggest impact on the surrounding plasma or at least produced the most visible (at 195Å) EUV wave. It also caused large active region loops to move towards the edge of the prominence cavity. Afterwards the loops swayed back and the cavity started to slowly (~ 2.5 km s^{-1}) but visibly expand over the next

3.5 hours. During this time the prominence rose into the cavity creating the tornado.

To understand the relationship between the flare, the prominence, the cavity and the tornado there are a number of effects that need to be considered. The expansion of the cavity is clearly associated with the rise of the prominence plasma. One possible explanation for the expansion is that the loss of free magnetic energy from the active region by flares and CMEs (Zhang & Low 2005) resulted in a contraction of the active region field, the Hudson effect (Hudson 2000; Zhang & Low 2003; Janse & Low 2007). Subsequently the surrounding fields, including the cavity field, expanded to fill the vacated space.

An idealized illustration of the Hudson effect, in terms of the force-free equilibrium between two bipolar fields before and after one of the fields has lost its free energy, is given in Fig. 8. Initially the active region field on the right has excess free energy, and the cavity field on the left is taken to be potential in order to simplify the calculation. During the eruption, the active region field loses free energy, decreasing its pressure since the magnetic energy density B^2 of a field $\mathbf{B}$ is also the magnetic pressure. This leads to an expansion of the cavity field to restore pressure balance in the system.

We consider the 2D Cartesian domain $0 < y < \pi$, $0 < z < \infty$, with x as an ignorable coordinate, taking the boundary to be a rigid perfect electrical conductor for simplicity. The initial state in Fig. 8a is a continuous global solution for the magnetic field, $\mathbf{B} = \mathbf{B}_{initial}$ of the force-free equations

$$\nabla \times \mathbf{B} = \alpha \mathbf{B} = 0; \quad \nabla \cdot \mathbf{B} = 0, \tag{1}$$

describing a bipolar ($\alpha = 0$) potential field representing the cavity that occupies the partial domain $0 < y < 2\pi/3, 0 < z < \infty$. This field continues into a constant-α force-free field representing the active region that occupies the complementary partial domain $2\pi/3 < y < \pi, 0 < z < \infty$. Their interface $y = 2\pi/3$, is in force balance because the fields on its two sides exert equal magnetic pressure. Suppose the electric current of the constant-α force-free field is removed from the partial domain $2\pi/3 < y < \pi, 0 < z < \infty$ to represent a flare-like loss of free energy. The distribution of the normal component of the field along the rigid boundary and the magnetic foot-points on the base $z = 0$ cannot change. This boundary condition then determine the unique end-state, $\mathbf{B}_{end}$, with $\alpha = 0$ everywhere in the domain (Fig. 8b). The former bipolar field on the right has contracted downward and withdrawn into a partial domain of a finite height while the other bipolar field now occupies the whole infinite space above that height. The fluid-interface between the two fields is now an arc of finite length. These mathematical solutions, given in the Appendix, serve to conceptually make specific a basic effect in the complex processes of a real energy release.

In addition to the active region contraction, the CME/flare eruptions generated hydromagnetic disturbances, seen as EUV waves, that perturbed the surrounding low corona. They evidently caused swaying in the prominence and oscillations along the cavity boundary. These perturbations may have been intense enough to partially destabilize the cavity-prominence system, thereby contributing to or possibly even initializing the tornado-like activity.

Our observational study supports the interpretation that the CME/flare activities in the active region had a
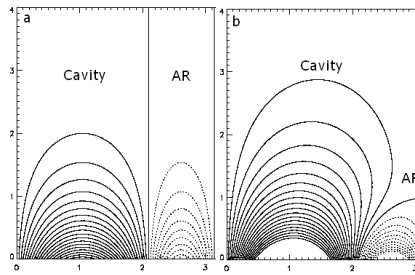

Fig. 8. Idealized 2D Cartesian magnetic fields of the cavity and active region (a) before and (b) after the flare, in a domain $0 < y < \pi, 0 < z < \infty$ with z denoting coronal height.

causal relationship with the nearby tornado. It is clear that the tornado was dynamically associated with the expansion of the prominence's helical field and its cavity. It is an open question as to whether the Hudson effect drove the cavity expansion and the helical field was responding dynamically to the expansion, or, the helical field loses its meta-stability as the result of hydromagnetic disturbances from the CME/flares from the active region. This physical question is worthy of MHD time-dependent simulation. Evidence of the Hudson effect has been reported in recent solar observational studies (e.g. Sun et al. 2012; Liu et al. 2009). Our study shows the importance of this effect in relation to CMEs, flares and prominences, and provides observational motivation for theoretical MHD modeling to address the specific questions posed by this relationship.

References

Attie, R., Innes, D. E., & Potts, H. E. 2009, A&A, 493, L13
Berger, T., Testa, P., Hillier, A., et al. 2011, Nature, 472, 197
Berger, T. E., Shine, R. A., Slater, G. L., et al. 2008, ApJ, 676, L89
Gibson, S. E., Foster, D., Burkepile, J., de Toma, G., & Stanger, A. 2006, ApJ, 641, 590
Gibson, S. E., Kucera, T. A., et al. 2010, ApJ, 724, 1133
Habbal, S. R., Druckmüller, M., et al. 2010, ApJ, 719, 1362
Halain, J.-P., Berghmans, D., Defise, J.-M., et al. 2010, in SPIE Conference Series, Vol. 7732
Howard, R. A., Moses, J. D., Vourlidas, A., et al. 2008, Space Science Reviews, 136, 67
Hudson, H. S. 2000, ApJ, 531, L75
Hudson, H. S., Acton, L. W., Harvey, K. L., & McKenzie, D. E. 1999, ApJ, 513, L83
Janse, Å. M. & Low, B. C. 2007, A&A, 472, 957
Lemen, J. R., Title, A. M., et al. 2012, Sol. Phys., 275, 17
Li, X., Morgan, H., Leonard, D., & Jeska, L. 2012, ApJ, 752, L22
Liggett, M. & Zirin, H. 1984, Sol. Phys., 91, 259
Liu, J., Zhou, Z., Wang, Y., et al. 2012a, ApJ, 758, L26
Liu, R., Wang, H., & Alexander, D. 2009, ApJ, 696, 121
Liu, W., Ofman, L., Nitta, N. V., et al. 2012b, ApJ, 753, 52
Low, B. C., Berger, T., Casini, R., & Liu, W. 2012a, ApJ, 755, 34
Low, B. C., Liu, W., Berger, T., & Casini, R. 2012b, ApJ, 757, 21
Mackay, D. H., Karpen, J. T., Ballester, J. L., Schmieder, B., & Aulanier, G. 2010, Space Sci. Rev., 151, 333
Martin, S. F. 1998, Sol. Phys., 182, 107
Pettit, E. 1943, ApJ, 98, 6
Régnier, S., Walsh, R. W., & Alexander, C. E. 2011, å, 533, L1
Su, Y., Wang, T., Veronig, A., Temmer, M., & Gan, W. 2012, ApJ, 756, L41
Sun, X., Hoeksema, J. T., Liu, Y., et al. 2012, ApJ, 748, 77
Tandberg-Hanssen, E., ed. 1995, Astrophysics and Space Science Library, Vol. 199, The nature of solar prominences
Thompson, W. T. 2009, Icarus, 200, 351
van Ballegooijen, A. A. & Cranmer, S. R. 2010, ApJ, 711, 164
Wedemeyer-Böhm, S., Scullion, et al. 2012, Nature, 486, 505

Zhang, M. & Low, B. C. 2003, ApJ, 584, 479
Zhang, M. & Low, B. C. 2005, ARA&A, 43, 103

Appendix A: Mathematical Illustration of the Hudson Effect

We give the mathematical solutions for 2D magnetic fields in Fig. 8, which are straight forward to construct by standard techniques. Use the representation

$$\mathbf{B} = \left[Q, \frac{\partial A}{\partial z}, -\frac{\partial A}{\partial y} \right], \tag{A.1}$$

in terms of the scalar flux-function $A(y, z)$ and the component $B_x = Q(y, z)$ corresponding to the ignorable coordinate x. The initial field $\mathbf{B}_{initial}$ in Fig. 7a is given by $A = A_{initial}$ and $Q = Q_{initial}$ where

$$A_{initial} = A_{pot} = 2\sin\left(\frac{3}{2}y\right)\exp(-\frac{3}{2}z); \quad Q_{initial} \equiv 0, \quad \text{in } 0 < y < 2\pi/3, 0 < z < \infty$$

$$A_{initial} = A_{fff} = -\sin(3y)\exp(-\frac{3}{2}z); \quad Q_{initial} = \sqrt{\frac{27}{3}}A, \quad \text{in } 2\pi/3 < y < \pi, 0 < z < \infty. \tag{A.2}$$

The end-state field $\mathbf{B}_{end}$ is the everywhere-potential field with $A = A_{end}$ where

$$A_{end} = \sum_{n=1}^{\infty} a_n \sin ny \exp(-nz), \tag{A.3}$$

$$a_3 = \frac{1}{3} \quad \text{and} \quad a_n = \frac{2 \times 3^4}{\pi} \sin\frac{2\pi n}{3} \frac{1}{(4n^2 - 9)(n^2 - 9)}, \quad \text{for } n \neq 3, \tag{A.4}$$

with $Q \equiv 0$. Both $\mathbf{B}_{initial}$ and $\mathbf{B}_{end}$ have the same distribution of normal field component along the boundary of the domain $0 < y < \pi$, $0 < z < \infty$.